Applied Surface Science 538 (2021) 148137

Contents lists available at ScienceDirect

Applied Surface Science

journal homepage: www.elsevier.com/locate/apsusc

Cation-exchange mediated synthesis of hydrogen and sodium titanates heterojunction: Theoretical and experimental insights toward photocatalyic mechanism

Isabela M. Iani[a], Vinícius Teodoro[b], Naiara L. Marana[c], Ubirajara Coleto Jr.[d], Julio R. Sambrano[c], Alexandre Z. Simões[e], Marcio D. Teodoro[f], Elson Longo[b], Leinig A. Perazolli[a], Rafael A. C. Amoresi[e,*], Maria Aparecida Zaghete[a]

[a] LIEC – Chemistry Institute, São Paulo State University – UNESP, 14800-060 Araraquara, SP, Brazil
[b] LIEC – Departament of Chemistry, São Carlos Federal University – UFSCar, 13565-905 São Carlos, SP, Brazil
[c] Modeling and Molecular Simulations Group, Sao Paulo State University, UNESP, 17033-360 Bauru, SP, Brazil
[d] Departament of Chemistry, Federal Institute of São Paulo – IFSP, 15808-305 Catanduva, SP, Brazil
[e] Faculty of Engineering of Guaratinguetá – UNESP, 12516-410 Guaratinguetá, SP, Brazil
[f] Department of Physics, São Carlos Federal University – UFSCar, 13565-905 São Carlos, SP, Brazil

ARTICLE INFO

This article is dedicated to Professor Dr. Maria A. Zaghete, whose commitment, teachings, scientific criticality, and extensive work has resulted in the training of countless researchers and articles that have further developed Science.

Keywords:
Heterojunction
Nanotubes
Charge carrier transfer mechanism
Z-scheme

ABSTRACT

$Na_2Ti_3O_7/H_2Ti_3O_7$ heterojunction nanotubes were obtained through the microwave-assisted hydrothermal method (MAH) with different band gap energy engineering. This study aimed to synthesize sodium titanate nanotubes and evaluate the influence of H^+ insertion on their photocatalytic properties. Heterojunctions were identified by X-ray diffraction, Raman spectroscopy and high-resolution transmission electron microscopy, and their electronic levels and defects were investigated using diffuse reflectance and photoluminescence spectroscopies in the UV–Vis region. The cation exchange process promotes the formation of $Na_2Ti_3O_7/H_2Ti_3O_7$ heterojunction with coexistence of both phases in the nanotube. Photocatalytic results of Rhodamine-B (Rh-B) dye discoloration show that the prepared materials have activity under visible and UV light irradiation, and are dependent on the proportion of hydrogen and sodium-titanate phases present. The material with highest sodium concentration showed discoloration with a half-life time of 23 min under visible light irradiation. Theoretical results reveal the heterojunction band offset as a staggered gap, with the effective bandgap occurring between the O-2p of $Na_2Ti_3O_7$ and Ti-3d of $H_2Ti_3O_7$. The charge carrier transfer mechanism in the heterojunctions is well described by Z-scheme, with $H_2Ti_3O_7$ and $Na_2Ti_3O_7$ as the main oxidation and reduction phases for dye discoloration.

1. Introduction

Considering that pollution levels have been increasing with measurable concentrations of the most diverse micropollutants [1,2], such as non-steroidal anti-inflammatory drugs [1], pesticides and herbicides [2], and textile dyes [3,4], it is necessary to study and develop environmentally friendly devices. Nanotubes are yielding unusually brilliant results in the diversified research area such as overall water splitting [5–7], electrode for batteries [8–10], gas sensor [11–13], supercapacitor [14–17] and environmental renovation [18–20]. Hydrogen titanate nanotubes and sodium titanates are promising as photocatalysts precisely due to their physicochemical properties, strong solar-light absorption ability, high photogenerated charge carriers' separation rate and flexible energy band structure, and have been studied mainly in the depollution of the environment [18–24] and obtaining renewable energy [25–27].

Titanates nanostructures have layered structures and high specific surface area [28,29]. The different compositions are related to the method of synthesis, such as sol–gel process, electrochemical (anodic) oxidation, or by alkaline hydrothermal treatment. The experimental parameters of these methods - temperature, time, pH or reagents used, are also related to the different compositions and their properties [30]. One of the methods used for the synthesis of one-dimensional nanostructures, nanotubes, is the microwave-assisted hydrothermal (MAH) method. This has the advantage of using relatively low temperatures and short reaction times [31,32], thus improving the cost-effectiveness

* Corresponding author.
E-mail addresses: rafaelciola@yahoo.com.br, rafael.ciola@unesp.br (R. A. C. Amoresi).

https://doi.org/10.1016/j.apsusc.2020.148137
Received 2 July 2020; Received in revised form 17 September 2020; Accepted 9 October 2020
Available online 15 October 2020
0169-4332/

of processing and allowing to study the growth kinetics of the particles. In this method, there are several parameters that can influence the growth, organization and shape (morphology) of the nanoparticles [33,34], influencing the electronic conduction properties of the semiconductors.

A way to optimize the photocatalytic properties of titanate nanotubes is to manufacture a photocatalyst with heterojunction structure, which acts directly on the photocatalysis mechanism through its charge carriers transport mechanisms. Photocatalysts that shows the Z-scheme mechanism have been attracting interest from researchers due to their stronger redox capacity when compared to a conventional type II heterojunction photocatalyst [35]. In the Z-scheme, more positive potentials of valence band (VB) and more negative of conduction band (CB) can improve the transfer of charged species (e^-/h^+) with strong oxidation and reduction capacities. This type of system shows an improved separation of the charge carriers which, consequently, improve the photoactivity of the materials [36–39].

Regarding TiO_2-derived nanotubes, which have titanium oxide as their precursor material to form the nanotube, there are some studies in literature related to the mechanism of formation and composition of such structures according to the medium in which their synthesis is carried out [32,40,41]. According to the desired morphology, temperature and reaction time of syntheses are well defined in literature [42,43]. Suetake *et al.* [44] and Hu *et al.* [45] observed structural and morphological changes in the synthesized materials when subjected to thermal treatments at different temperatures, and they directly affect the mechanism and the photodegradation efficiency of the material. In addition, studies show that the particle size and composition of titanate directly influences the photocatalytic properties. Sodium titanate nanotubes showed high photocatalytic efficiency under UV light irradiation [23]. Sandoval *et al.*[4] studied the degradation of methylene blue dye by TiO_2-derived nanotubes and evaluated the photocatalytic activity under UV irradiation, assigning its efficiency mainly to the hydrogen titanate phase. For the nanotubes obtained by this method, the presence of both phases (hydrogen and sodium titanate) is verified [4,46]. However, a discussion regarding the interface effects between these phases is poorly studied in literature, and in this work our main goal is to investigated a material that has two different crystalline phases in its structure.

Recent investigations of phases and facet engineering of semiconductor crystals have shown that the optical activity is not only dependent on the physical and chemical properties of the catalyst, but also on the correlation of the externally exposed crystal surface, that is, on the arrangement and construction of the atomic surface [47–50]. Therefore, analyzing the concomitant presence and interfacial effects of both phases of titanate (heterojunction) in photocatalytic activity is of fundamental importance for improvement and modelling of materials with desirable properties.

This work shows a study of nanotubes with the presence of two phases of titanates, with photocatalytic activity under visible and UV light irradiation. Experimental analyses using scanning and transmission electron microscopies (SEM and TEM), X-ray diffraction (XRD), Raman scattering spectroscopy, diffuse reflectance spectroscopy (DRS), photoluminescence emission spectroscopy (PL) together with theoretical analyses using density functional theory (DFT) reveal the composition, morphology and structure (crystalline and electronics) of the prepared materials. Such analyses were applied in order to explain the differences in the photocatalytic response observed by the content of different phases of the titanates nanotubes.

2. Experimental procedure

2.1. Preparation of titanate nanotubes

The nanotube syntheses were perfomed by the microwave-assisted hydrothermal (MAH) method. The procedure started with the preparation of a suspension with commercial TiO_2 (VETEC 98%) dispersed in 10 M aqueous NaOH solution [51] and taken to the microwave heat treatment after 1 h in magnetic stirring at 25 °C. The synthesis temperature was fixed at 180 °C, with a maximum pressure of 148 psi, heating time of 7 °C.min^{-1} and synthesis time of 1 h, under power of 450 W.

The alkaline powders obtained were subjected to two types of washes: successive washes with deionized water until reaching a neutral pH, that is, gradually decreasing the initial pH from 14 to 7, obtaining nanotubes (NT) named as "NT-H_2O" sample; and alternating washes with deionized water and a 0.1 M HCl solution, until reaching neutral pH, resulting in nanotubes named as "NT-HCl" sample. At the end, another wash with ethanol was made for both samples and the powders were dried at 60 °C.

2.2. Titanate nanotubes characterization

The morphology of the samples was analyzed by field-emission scanning electron microscope (FE-SEM) in FE-SEM JEOL® model 7500F equipment, and by TEM analysis in a FEI TECNAI G2 F20 HRTEM® microscope. Crystallinity was evaluated by XRD using the Rigaku® diffractometer, model RINT2000, with 2θ angular scanning from 20 to 80°, Cu Kα radiation (λ = 1.5406 Å). To determine the vibrational modes and obtain information of the structures at short range, Raman scattering spectroscopy was performed using a LabRAM iHR550 (Horiba Jobin Yvon), with a He-Ne laser of λ = 632.8 nm, obtaining scattering spectra in the range from 50 to 1000 cm^{-1} with a Silicon (Si) charge-coupled device (CCD, Synapse). Porosity and specific surface area were evaluated by a Micrometrics ASAP specific surface meter, using adsorption-dessorption isotherms of N_2 physisorption, according to the method of Brunauer, Emmett, Teller (B.E.T).

Optical characterizations were made for obtaining the gap energy of the samples through diffuse reflectance measurements in an absorption spectrophotometer in the UV–Vis region with an integrating sphere of 150 mm in diameter with InGaAs detectors, in the Lambda 1050 model from Perkin Elmer. From the diffuse reflectance spectra obtained, it is possible to calculate the bandgap energy (E_g) of the samples, considering the Kubelka-Munk remission function (Equation (1)), which is proportional to the absorption coefficient of the material, described in Equation (2). The Tauc plot determines the bandgap energy (E_g) of the samples from the intercept on the abscissa axis of a linear fit of the $(\alpha h\nu)^{1/2}$ vs $h\nu$ plots, where α is the absorbance and $h\nu$ the photon energy, considering an indirect bandgap for sodium and hydrogen titanates. From the values of E_g found, their corresponding wavelengths (λ) were calculated using Equation (3).

$$F(R) = (1 - R^2)/2R \propto \alpha \quad (1)$$

$$(\alpha h\nu)^r = K(h\nu - E_g) \quad (2)$$

$$E = h\nu/\lambda \quad (3)$$

In the equations described above *F(R)* is the Kubelka-Munk function, *R* is the reflectance value, *E* is the bandgap energy in eV, *h* is the Planck constant (4.136×10^{-15} eV.s), ν is the speed of light (2.998×10^8 m.s^{-1}) of the incident photon and the exponent r can have values ½ and 2 representing the indirect and direct transition, respectively. Assuming the indirect transition, it is evident that, when plotting $(\alpha h\nu)^{1/2}$ as a function of $h\nu$, it is possible to calculate E_g by extrapolating the linear region to $(\alpha h\nu)^{1/2} = 0$.

In order to explore the electronic transitions and investigate the nature of the defects within the materials, microphotoluminescence spectroscopy were employed by means a home made confocal microscope using as excitation source a 355 nm laser (Cobolt/Zouk) coupled to a single mode optical fiber, with the beam focused on the sample by an aspheric lens (WD = 1.6 mm and NA = 0.64). Neutral density filters were used to control the laser power. The luminescence was collimated

by the same lens and magnified into a 50 μm multimode optical fiber. The backscattered laser beam was blocked using an superedge filter, and the luminescence was dispersed by a diffraction grid of 150 lines/mm contained within a 75 cm spectrometer (Andor/Shamrock) and detected by a Si-CCD (Andor/Idus).

2.3. Photocatalytic experiments

The photocatalytic tests were performed in a photoreactor maintained at a temperature of 28 °C with a thermostatic bath, with air bubbling (10 $mL.min^{-1}$) under two irradiation conditions: UV light (λ = 254 nm), with Osram® lamp Puritec HNS 2G7, 11 W, and visible spectrum light from a Philips TL-D commercial lamp, 15 W. The tests were performed in a Rhodamine-B (Rh-B) solution with a concentration of 0.01 $mmol.L^{-1}$ with 70 mg of suspended titanate nanotubes. In all tests, aliquots of the solution exposed to photocatalytic action were removed from time to time and analyzed with an absorption spectrophotometer Perkin Elmer Lambda 1050 region.

2.4. Theoretical methods

The titanates nanoparticles were theoretically studied by applying the Density Functional Theory, with the default WC1LYP hybrid functional [52]. All the calculations were made using the CRYSTAL17 program [53], which uses a Gaussian-type basis set to represent crystalline orbitals as a linear combination of Bloch functions defined in terms of local functions (atomic orbitals). The sodium, titanium, oxygen, and hydrogen atomic centers were described by all-electron basis set, 8-511G [54], 86–411(d31)G [55], 8-411d1 [56] and 5-11G* [57], respectively.

As a first step, the optimization of the lattice parameters and internal coordinates of $H_2Ti_3O_7$ and $Na_2Ti_3O_7$ were conducted to minimize the total energy of the structure at experimental parameters. In order to compare directly with the experimental results obtained in the present study, the theoretical structure for $H_2Ti_3O_7$ was obtained as belonging to the monoclinic C2/m space group, while the $Na_2Ti_3O_7$ was simulated as monoclinic $P2_1/m$. The optimized cell parameters obtained are a = 16.21, b = 3.76 and c = 9.50, with β = 99.62, for $H_2Ti_3O_7$; and a = 8.64, b = 3.81 and c = 9.21, with β = 101.79, for $Na_2Ti_3O_7$. The theoretical cell parameters are in agreement with the experimental and theoretical data [58–62].

From the optimized structures, the electronic properties were obtained. The band structures were obtained for 100 K points along the appropriate height-symmetry paths of the adequate Brillouin zone, and the Density of States (DOS) diagrams were calculated to analyze the corresponding electronic structure. Based on the electronic properties, the electronic transitions were evaluated by band alignment, considering the $H_2Ti_3O_7/Na_2Ti_3O_7$ heterostructure. Accordingly, the heterostructures can be classified as type-I and/or type-II behavior, depending on the band offset between the two materials. This analysis can help to explain the photocatalytic properties observed experimentally.

3. Results and discussions

3.1. Morphology and structure of titanate nanotubes

Figure S1 shows the images obtained by FE-SEM for samples prepared from commercial anatase TiO_2. It is observed that the spherical morphology presented by commercial TiO_2 (Figure S2), was changed to nanotube type morphology using the MAH synthesis method at 180 °C/1h, as shown in SEM, Figure S1, and supported by TEM images, Fig. 1. It is observed that the two samples differ in length and diameter size. The sample washed with 0.1 M HCl solution showed less agglomerated nanotubes compared to the sample washed only with deionized water, which is related to the effect of the interation between H^+ ions and the nanotube surface. The dimensions of the nanotube were calculated by average values measured from regions of the sample. For the NT-H_2O sample, the outer diameter obtained was 10.10 nm, the inner diameter of 5.07 nm (inserted in Fig. 1a) and the wall thickness of 2.51 nm. For the NT-HCl sample, the outer diameter was 9.20 nm; the inner diameter was 5.4 nm (inserted in Fig. 1b), and the wall thickness was 1.98 nm. Therefore, the NT-H_2O nanotubes have a larger external diameter and wall thickness than the NT-HCl nanotubes. It can also be observed spherical particles along the titanate nanotubes in the NT-HCl sample, Fig. 1b. To further investigate these particles, a HRTEM image was collected and is shown in Figure S3. According to the randomness of atoms composing this particle and the absence of fringes, it can be concluded that these particles are in the amorphous form and possible composed by titanium and oxygen atoms.

Fig. 2 shows an HRTEM image of NT-H_2O sample. According to the Fast Fourier Transform (FFT) analyses (inset) of the obtained nanotube, the presence of both titanate phases ($H_2Ti_3O_7$ and $Na_2Ti_3O_7$) were observed in the same nanotube particle. The TEM analyses were performed in DigitalMicrograph (Gatan) software by applying a mask filter in the FFT generated from the HRTEM image. Then the pattern was generated from inverse FFT and its frequency distribution was analyzed to obtain the crystalline interplanar distance. Due to the nanotube morphology, the HRTEM analyses can be performed only in its walls, which causes a relatively weak intensity of the points in the FFT analyses, as can be observed in Fig. 2. The formation of the heterojunction between both titanate phases was confirmed by TEM analyses, as observed by the interplanar distances of 7.89 Å related to the $H_2Ti_3O_7$ (200) plane and 8.45 Å related to the $Na_2Ti_3O_7$ (001) plane, both being the most intense planes in XRD patterns, according to ICSD n° 237,518 and ICSD n° 15463, respectively.

Since the HCl is a strong acid with a high dissociation constant, the washing process in the synthesis procedure results in a higher concentration of H_3O^+ in solution compared to the washing process with deionized water. The higher content of H_3O^+ in solution provides a higher content of H^+ to interact with suspended $Na_2Ti_3O_7$ nanotubes by a cation exchange reaction, thus forming $H_2Ti_3O_7$ phase [63]. This heterojunction with both phases in a same particle is characteristic of cation exchange reactions, indicating the effectiveness of the washing process to provide a higher content of H^+ for the formation of the heterojunction. The cation exchange method was also employed by Rivest *et al.*[64] to obtain nanorods with heterojunctions between Cu_2S and CdS, also observing the presence of both phases in the same particle. The cation exchange process by the washing process is represented in the Equation (4).

$$Na_2Ti_3O_7 + xHCl \rightarrow 1\text{-}xNa_2Ti_3O_7 + xH_2Ti_3O_7 + xNaCl \quad (4)$$

The specific surface area of the nanotubes is related to the outer and inner diameter and its thickness. It was observed that the nanotubes washed only with deionized water have a smaller surface area, 349.01 m^2/g, when compared to the nanotubes washed with the HCl solution, 505.73 m^2/g. In photocatalysis this is an important parameter for the efficiency of the material, since the larger the surface area, the greater its surface contact with the reaction medium.

Fig. 3a shows the XRD patterns for the NT-H_2O and NT-HCl samples and the standard cards of monoclinic phases of the sodium trititanate ($Na_2Ti_3O_7$, space group P121/m1, ICSD - n° 15463) and of the hydrogen trititanate ($H_2Ti_3O_7$, space group C12/m1, ICSD - n° 237518), and of the anatase phase of the titanium dioxide (TiO_2, space group I41/amdS, ICSD - n° 9852).

The XRD patterns have a profile consisting regarding two of the peaks group shown. The first group of peaks indicated in red dashed lines in the Fig. 3a, are located at 9.7°, ~ 28°, and 39.1° 2θ corresponding to the planes (100), (1–11), and (30–3) of the $Na_2Ti_3O_7$ phase, respectively. The second one, indicated in blue dashed lines in the image, is located at 9.2°, 24.2°, and 48.4° 2θ corresponding to the planes (001), (1–10), and (020) of the $H_2Ti_3O_7$ phase, respectively. In

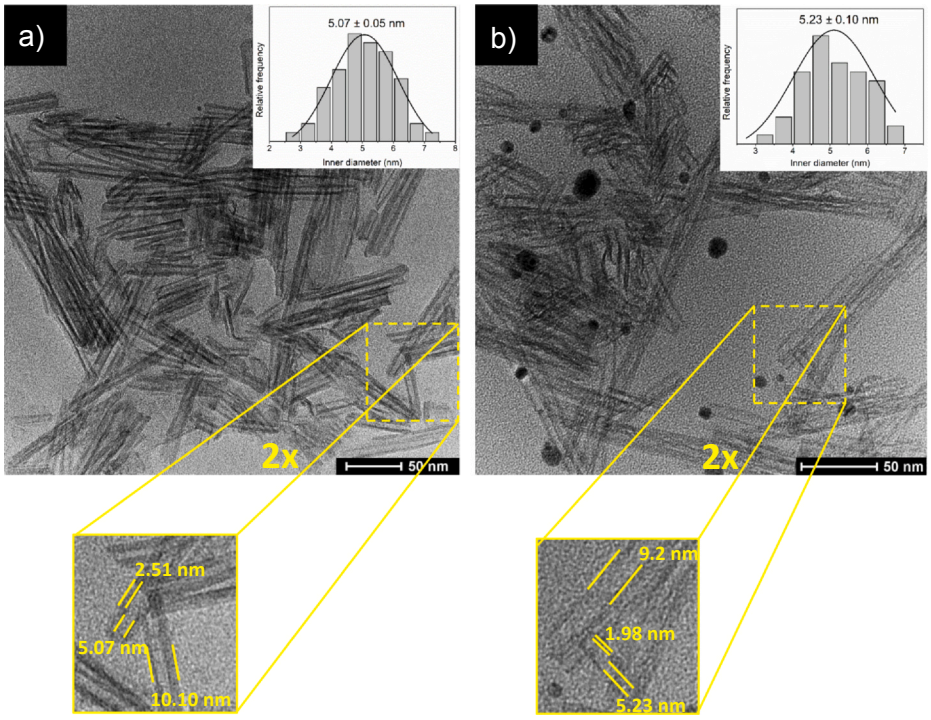

Fig. 1. TEM images of the titanates washed with **a)** water (NT-H_2O) and **b)** HCl solution (NT-HCl), showing the inner and outer diameter, and the wall thickness of the obtained nanotubes (inset).

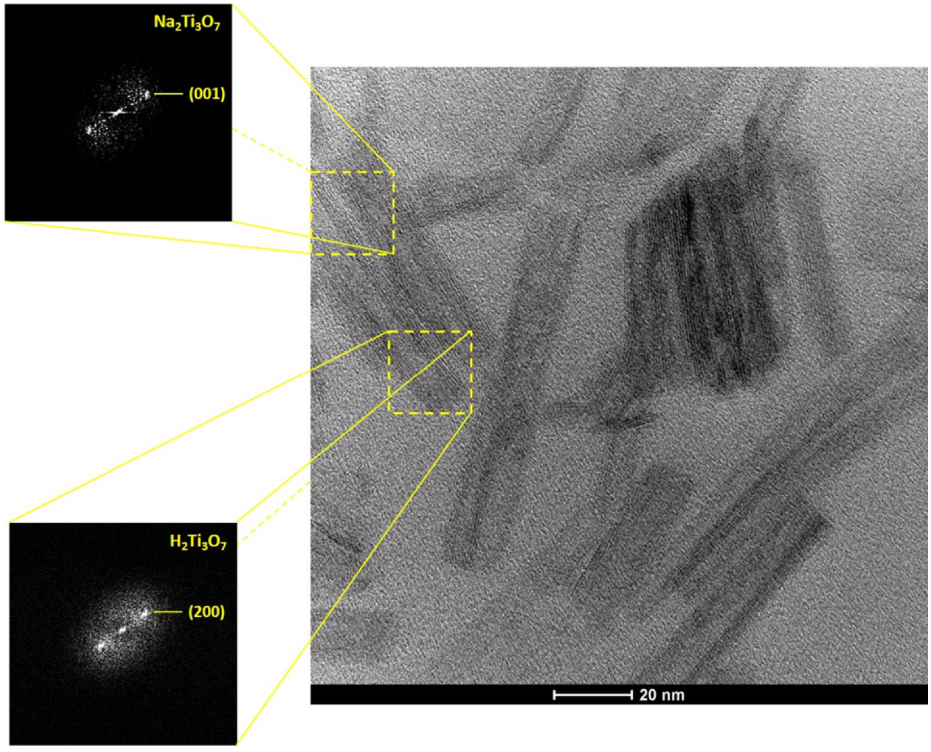

Fig. 2. HRTEM image of NT-H_2O with its FFT analyses (inset).

order to verify the presence of the precursor phase in the samples, the TiO_2 anatase phase pattern is also shown. By carefully checking the TiO_2 peaks, we can conclude that the main planes do not coincide with the diffracted peaks of the samples, discarding the presence of the anatase phase in the material composition. Therefore, XRD patterns of the samples indicate the monoclinic phases of the $H_2Ti_3O_7$ and of the $Na_2Ti_3O_7$.

The peak observed in the XRD patterns at ~ 9.5° has a wider profile due to the contribution of the (*h*00) planes of two phases. When comparing the patterns presented by the two samples, the presence of a peak at 61.2° referring to $Na_2Ti_3O_7$ phase [32] is noted only in NT-H_2O, showing that it has higher concentration of Na^+ ions into its lattice than in NT-HCl. Fig. 3a also shows displacements of the peaks located in the region of 10° and 28°. The NT-HCl sample has these peaks shifted to

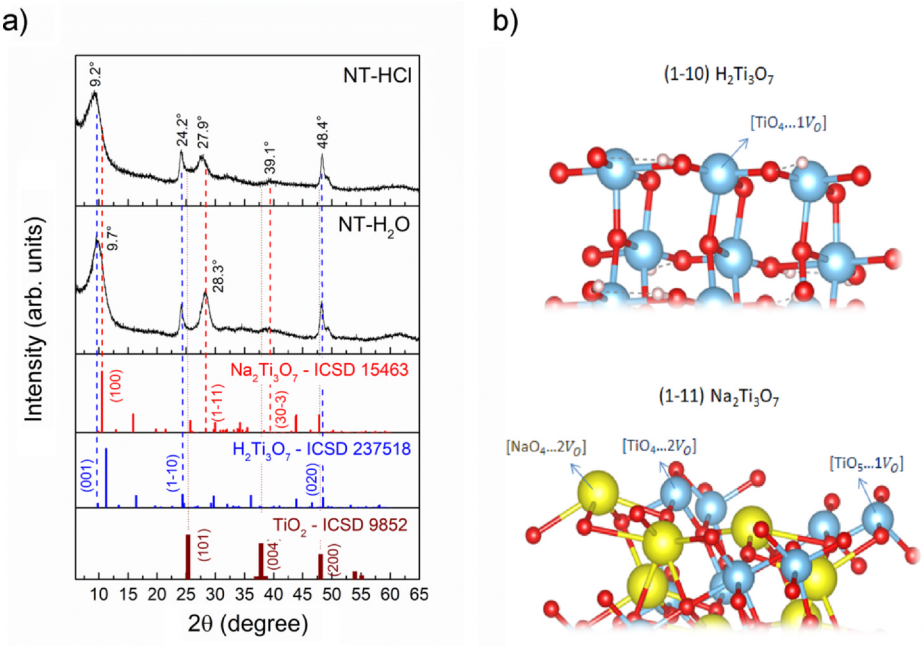

Fig. 3. a) XRD patterns of NT-H_2O and NT-HCl samples, in which the blue, red, and wine dashed lines indicate the planes of the $H_2Ti_3O_7$, $Na_2Ti_3O_7$ and anatase TiO_2 phases respectively, and **b)** arrangement of the surfaces (1–10) and (1–11) of the hydrogen and sodium titanate phases, respectively, showing the clusters belonging to each surface. (For interpretation of the references to colour in this figure legend, the reader is referred to the web version of this article.)

a smaller diffraction angle compared to the NT-H_2O sample. According to Bragg's Law, the decrease in the diffraction angle is a consequence of the increase in the distance of the atomic planes [65]. This observed displacement may be related to the difference in the concentration of Na^+ and H^+ ions in the crystalline lattice of the samples, related to the synthesis method of obtaining NT-HCl.

These findings are supported by the relative concentration of the sodium titanate phase, as shown in Table 1. The relative concentrations were calculated using the sum of the peaks' integrated intensities for each phase, according to the Equation (5) [66]. $\sum I^N$ and $\sum I^H$ are the sums of the peaks integrated intensities of the sodium titanate phase and hydrogen titanate phase, respectively. There was a 22% reduction in the sodium titanate phase content for the NT-HCl sample compared to the NT-H_2O sample. A change in the relative intensities of

(1–11) and (1–10) planes in the samples, which belong to $Na_2Ti_3O_7$ and $H_2Ti_3O_7$, respectively, was observed. As shown in Fig. 3a, the sample washed with deionized water presented a higher intensity of (1–11) plane than (1–10), thus inverting the relative intensity of these planes for washing with HCl, indicating a higher proportion of $H_2Ti_3O_7$ in the NT-HCl sample than the NT-H_2O sample. Futhermore, this change in diffraction plane intensity implies a difference in the surfaces exposed in the nanotubes [67,68]. As can be seen in Fig. 3b, the (1–10) plane of the hydrogen titanate phase has atomic surface coordination of $TiO_4.1V_O$ type, whereas the (1–11) plane has several types of cluster coordinations increasing the level of surface defects [69]. This will result in different interactions in the photocatalytic mechanism as discussed in the following topics.

$$\text{Relative concentration}(\%) = \sum \text{IN}/(\sum \text{IN} + \sum \text{IH}) \quad (5)$$

The short-range changes in the crystalline structure of the obtained nanotubes were investigated by Raman spectra, Fig. 4. From the obtained spectra it is possible to denote modes related to stretching of distorted octahedron [TiO_6] clusters, Na…O–Ti bending mode, and

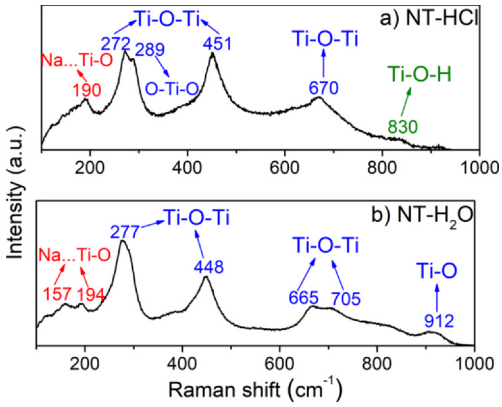

Fig. 4. Raman spectra of nanotubes: **a)** NT-HCl and **b)** NT-H_2O samples. The position and types of scattering of the Raman bands are indicated by arrows within the image.

covalent Ti–O–H bonds, as shown in Table 2. Regarding the active modes, there are a greater number of modes for the NT-H_2O sample (Fig. 4b) compared to the NT-HCl sample (Fig. 4a). Similar vibrational modes were found between the samples. For the NT-HCl sample there was a suppression of the bands located at 157 cm^{-1} and 912 cm^{-1}, related to the Na…Ti–O bending mode and the short Ti–O bond in the distorted octahedron [TiO_6] near to Na ion of the nanotubular structures, respectively. Also, there was a higher definition of the band at 289 cm^{-1} related to the stretch Ti–O–Ti in an octahedral chemical environment of [TiO_6] [70] and disappearance of the band at 705 cm^{-1} assigned to the Ti–O–Ti flexion modes. The suppression of these modes, the better definition of the bands, as well as the amount of active vibrational modes for the NT-HCl sample indicate: i) effective cation exchange of Na^+ for H^+ through the washing process of the samples

Table 1
XRD results for NT-H_2O and NT-HCl samples.

Sample	Σ Peaks Intensities of $Na_2Ti_3O_7$	Σ Peaks Intensities of $H_2Ti_3O_7$	Relative Concentration of $Na_2Ti_3O_7$ phase	Relative Concentration of $H_2Ti_3O_7$ phase
NT-H_2O	2783	1119	71%	29%
NT-HCl	1524	1614	49%	51%

Table 2
Attribution of Raman modes for the nanotubes and the respective comparisons with the literature.

NT-H_2O Raman shift (cm^{-1})	**NT-HCl** Raman shift (cm^{-1})	**Attribution**	**References** Raman shift (cm^{-1})
157	–	Na… O–Ti bending	160 [74,73]
194	190	Na… O–Ti bending	195 [74], 196 [73]
277	272	Ti–O–Ti stretching in edge-shared TiO_6 units	278 [74], 280 [73], 276 [72]
–	289	O-Ti-O stretching	286 [75]
448	451	Ti–O–Ti stretching in edge-shared TiO_6 units	448 [74], 454 [73]
665	670	Ti–O–Ti stretching in edge-shared TiO_6 units	656 [74] 663 [73]
705	–	Ti–O–Ti flexion modes	706 [74]
–	830	covalent Ti–O–H bond	822 [72], 830 [72]
912	–	short Ti–O bonds in the distorted TiO_6 octahedron	906 [74], 905 [73], 917 [71]

[71,72] ii) increased participation of Ti–O terminal bonds where the oxygen is unshared between [TiO_6] clusters [73] and iii) an increase in symmetry in the nanoparticle with the smaller number of active Raman scattering modes [72]. Therefore, corroborating with those results found in the XRD analyses, there are long and short-range changes in the crystalline structure of the samples, which represent a direct influence on the transport of charge carriers in the semiconductor.

3.2. Identification of optical and electronic characteristics

Fig. 5 shows the Tauc plots of the NT-H_2O and NT-HCl samples, which were plotted from correlation between their diffuse reflectance data and their absorbance by Kubelka-Munk algorithm (Equations 1–3) [76]. For both samples, the Tauc plot shows the formation of two inflection points in their spectra. This behavior indicates electronic transitions between the valence and conduction band of distinct crystalline phases in the material. Herein, the appearance of two band gap values for the NT-H_2O and NT-HCl samples, which are registred in Table 3, confirmed the heterojunction formation in these samples, supporting the TEM analyses. For the NT-H_2O sample, the obtained band gap values were 3.02 eV and 3.38 eV, as represented in Fig. 5a. The first value corresponds to an absorption edge wavelength of 411 nm in the visible region, and the second one corresponds to a absorption edge wavelength in 367 nm, corresponding to the UV region. For the NT-HCl sample, the band gap values found were 2.46 eV and 2.93 eV, corresponding to absorption edge wavelengths of 504 nm and 423 nm, respectively, comprising part ofthe visible region, Fig. 5b. Since the $H_2Ti_3O_7$ phase presents a lower value of band gap energy than $Na_2Ti_3O_7$, as previously reported by other studies [77,25], the lower values for both NT-H_2O and NT-HCl samples can be assigned to the $H_2Ti_3O_7$ phase and the higher values for the $Na_2Ti_3O_7$ phase. Since three of the four values correspond to band gap energies visible (above 410 nm) the materials may present photoactivity under visible irradiation.

Fig. 6 shows the PL emission spectra of the samples. It was observed for both samples that the optical recombination comes from different energy levels inside the bandgap region, most likely from defects

Table 3
Bandgap energy values and their respective absorption edge wavelengths found for the samples.

Samples	λ_1 (nm)	E_g (eV)	λ_2 (nm)	E_g (eV)
NT-H_2O	411	3.02	367	3.38
NT-HCl	504	2.46	423	2.93

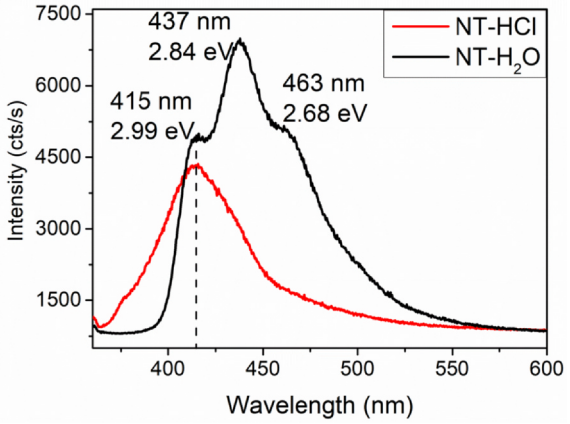

Fig. 6. Photoluminescent emission spectra of nanotubes washed with H_2O and HCl.

centers, pushing the recombination energy to the visible spectral range. The spectrum of the NT-H_2O sample shows a broad band with peaks with maximum intensities at 415 nm, 437 nm and 463 nm, corresponding to the energies of 2.99 eV, 2.84 eV and 2.68 eV, respectively. The NT-HCl sample spectrum consists of a more narrow band with a maximum peak at 415 nm (2.99 eV) and a tail extending to ~ 500 nm. The broad bands obtained in the PL spectra are characteristic of multiphononic processes, that is, processes in which the emission occurs through several paths due to the high density of electronic states within the band gap region. This allows the momentum electron to relax in the

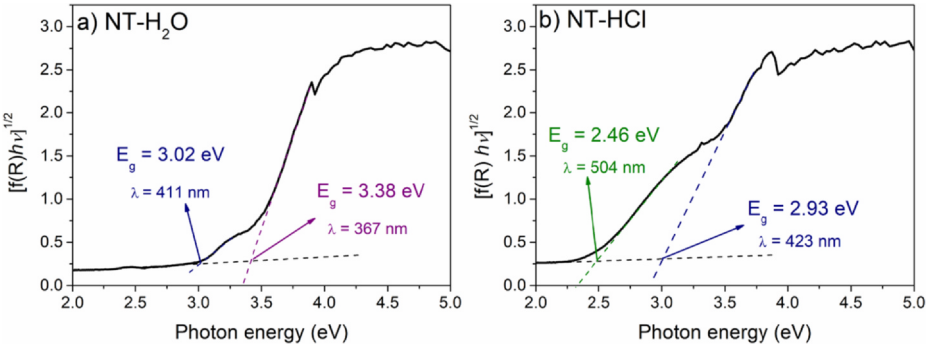

Fig. 5. Tauc plot of the **a)** NT-H_2O and **b)** NT-HCl samples.

form of a non-radiative process before its radioactive recombination [78].

Photoluminescent emissions involve radiative electronic transitions that occur due to the excitation of charged carriers, which emit electromagnetic radiation in the form of photons when returned to their fundamental state [34]. This phenomenon is determined according to the band structure of each material, including the formation of energy level states in the band gap due to structural distortions and defects. This can contribute to the radiative emission with a high energy difference between these levels, increasing the radiactive contribution [78]. Therefore, in these cases, the degree of structural disorder/defect is usually inversely proportional to the rate of recombination of the electronic carriers, and consequently, the emission intensity is higher [79]. Thus, relating the higher intensity emission spectrum of the NT-H_2O sample to its structural characteristics discussed in the previous sections, it is confirmed that this material has a more disordered crystalline structure compared to the NT-HCl sample. For the photocatalytic effects of the materials studied, the electron-hole recombination rate is an important parameter, since the lower the recombination rate, the higher the availability of charge carriers to initiate the oxireduction reactions of organic compounds and dissolved species.

The structural defects that are largely related to the wide-range emission of the visible spectrum are oxygen vacancies of doubly $V_{\ddot{O}}$ and mono $V_{\dot{O}}$ ionized types. Both vacancy types work as sites for capturing excited electrons in their decay. As they become trapped in these defects, photons of specific wavelengths are emitted, corresponding to the energy difference between electronic levels.

To analyze the contribution of such defects in the structure of the materials for the emitted wavelengths, deconvolutions of their emission spectra were perfomed with Voigt area function, as presented in Fig. 7.

For the NT-H_2O sample (Fig. 7a) a small band was found in the UV region (360 nm) and two bands that emit in the violet region (415 and 439 nm) which represent 58.47% of the emission. These emissions types is related to the band-to-band radiative decay, due to the direct recombination of the electronic carriers between the conduction and valence bands [80,81]. The two emission wavelengths of the violet region are related to band gap energy values found in UV–Vis analysis, confirming the existence of two different materials in the same sample, presenting different energy levels. There are also bands in blue (464 nm), cyan (486 nm) and green (509 nm), which are related to the existence of $V_{\dot{O}}$ monoionized oxygen vacancies [78]. This type of defect is energetically located close to the valence (type-p) or conduction bands (type-n), which are denominated as shallow defects and represent high energy emissions (blue-green) [82]. Double-ionized oxygen vacancies $V_{\ddot{O}}$ are energetically closer to the Fermi level, so they are classified as deep defects and correspond to low energy emissions (yellow–red) [80]. Fig. 8a shows the proposed mechanism for the PL emission of this material, considering the large band gap previously found. The possible paths of electronic transitions for PL emission can be observed, which are formed by the energy levels of the defect states within the band gap region.

In the deconvolution on PL spectrum of the NT-HCl sample (Fig. 7b), an intense and wide band was found in the violet region (414 nm) that represents 74.84% of the total emission. The emissions in violet (greater energy), are related to the direct radiative decay of the electronic carriers [81,82]. This percentage increase in relation to NT-H_2O indicates that it has a lower proportion of defect states in its band gap, which hinders the direct recombination, resulting in a greater participation of these states in the total emission in NT-H_2O than in the NT-HCl sample. In the PL spectrum of the NT-HCl sample, there are also bands in blue (450 nm), cyan (487 nm) and green (535 nm) regions, however with lower intensities. Fig. 8b shows the proposed mechanism for the PL emission of this material, considering the large band gap previously found. The energy levels of the defect states and the possible paths of electronic transitions for PL emission are demonstrated. The broader PL band of NT-H_2O with a higher contribution of oxygen vacancies for the emission are well expected and predicted by theoretical simulations, as described earlier in Fig. 3b. Since the NT-H_2O sample has a higher proportion of $Na_2Ti_3O_7$ phase than the NT-HCl sample, and this phase presents a higher proportion of oxygen vacancies as observed by the (1–11) surface termination than the (1–10) surface termination of $H_2Ti_3O_7$, it is well expected that the sample with higher proportion of $Na_2Ti_3O_7$ phase , *i.e.* NT-H_2O presents a higher contribution of oxygen vacancies and hence a broader band in PL emission.

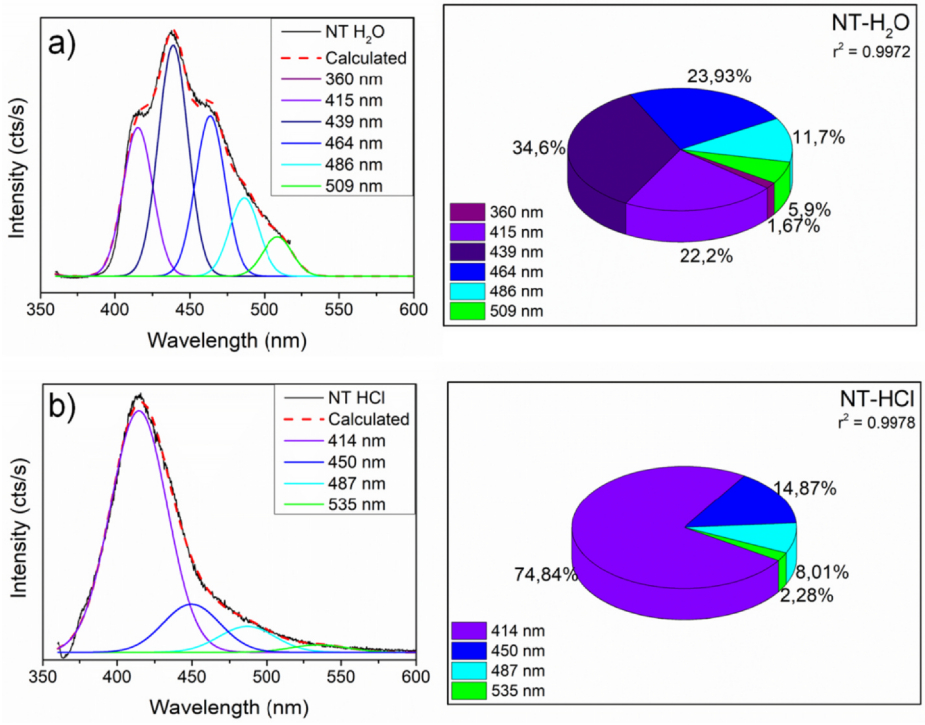

Fig. 7. Deconvolution of the PL spectra of **a)** NT-H_2O and **b)** NT-HCl samples.

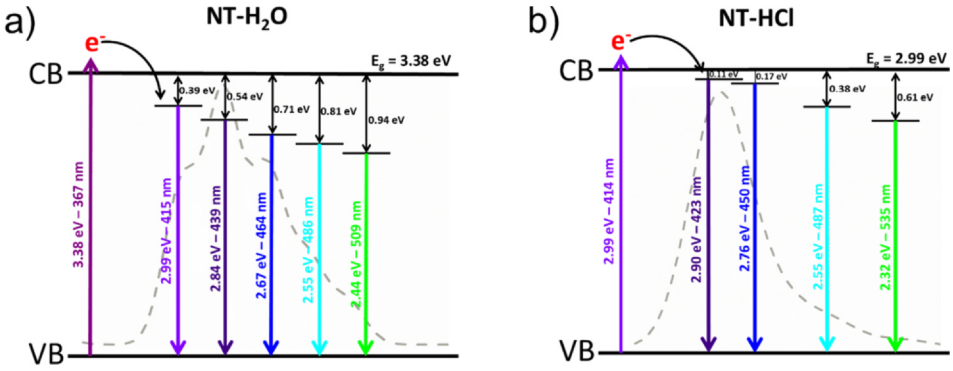

Fig. 8. Scheme of energy decay of the PL deconvolutions for the **a)** NT-H_2O and **b)** NT-HCl samples.

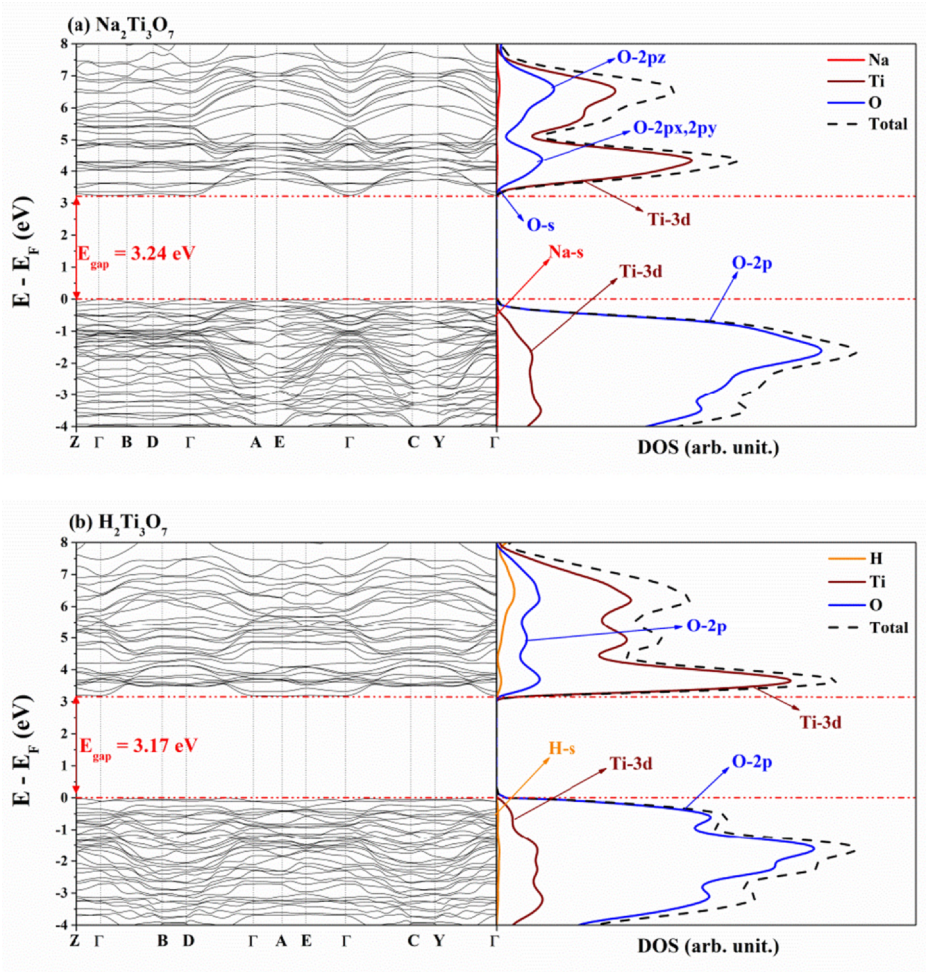

Fig. 9. Band structures and density of states for **a)** $Na_2Ti_3O_7$ and **b)** $H_2Ti_3O_7$.

The band structure and DOS are shown in Fig. 9. It can be observed that, for $H_2Ti_3O_7$ the band gap is 3.17 eV and it is indirect between Γ-B points, while for $Na_2Ti_3O_7$ the bandgap is direct, 3.24 eV, at Γ point. These results agree with the results available in the literature and corroborate with the lower band gap value of $H_2Ti_3O_7$ than $Na_2Ti_3O_7$ phases obtained experimentally and analyzed by diffuse reflectance spectroscopy [61,62]. The DOS analyses reveal that the main contributor at VB for both materials is the oxygen. The 2p valence orbitals are the greater contributors in this region and at the bandgap area. It is interesting to note that, for both materials, the sodium and hydrogen atoms have a minimum contribution over the entire energy range, being more prominent in the innermost CB. As expected, the titanium atoms have a great contribution at CB, and the 3d orbitals have a high-density state in this energy range. For both materials, the electronic transition is expected to occur between the O-2p of the VB and the Ti-3d of the CB.

3.3. Photocatalytic tests

Fig. 10a shows the results of Rh-B photodiscoloration using the two photocatalytic samples and the reaction time under UV and visible light irradiation. Fig. 10b shows pseudo-first order kinetic plot of photodiscoloration curves. A pseudo first order reaction rate law is assigned as $[\ln(A_0/A_t) = kt]$, in which the slope of the fitting line is the value of

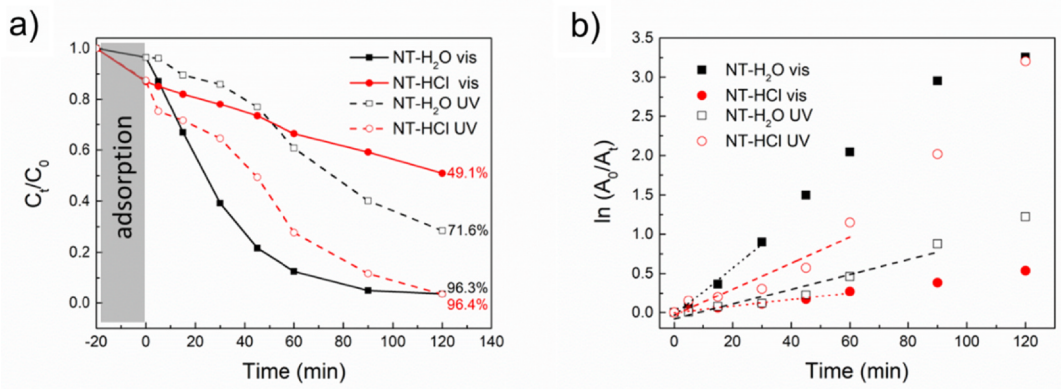

Fig. 10. a) Photodiscoloration efficiency of Rh-B under UV and visible irradiation and **b)** Pseudo-first order kinetic plot of photodiscoloration curves for NT-H_2O and NT-HCl samples.

Table 4
Photocatalytic results and kinetic parameters of the photodegradation reactions.

Radiation	Parameter evaluated	NT-H_2O	NT-HCl
	Composition	↑ $[Na]^+$	↓ $[Na]^+$
UV	% Degradation	71.6%	96.4%
	K	9.50×10^{-3} min^{-1}	1.66×10^{-2} min^{-1}
	$t_{1/2}$	73.0 min	41.8 min
Visible	% Degradation	96.3%	49.1%
	K	3.03×10^{-2} min^{-1}	4.28×10^{-3} min^{-1}
	$t_{1/2}$	22.8 min	162.0 min

the rate constant, k. Substituting this constant in [(ln 2) / k], the half-life time of photodiscoloration ($t_{1/2}$) was obtained [83].

The calculated reaction rate constant and the half-life time of the photodegradation are presented in Table 4. For all photocatalytic experiments, the results are in well agreement with the pseudo-first order kinetic, according to the Langmuir-Hinshelwood model [84]. For UV irradiation the NT-HCl sample showed a 25% higher discoloration than NT-H_2O sample. The photocatalysts irradiated by visible light showed the opposite behavior, the NT-H_2O sample showed a 47% higher photocatalytic efficiency than the NT-HCl sample. As expected, the faster photodiscoloration was found for the reaction with NT-HCl ($k = 1.66 \times 10^{-2}$ min^{-1}) under UV irradiation and with NT-H_2O ($k = 3.03 \times 10^{-2}$ min^{-1}) under visible light irradiation, which consequently had the shortest half-life times of 42 and 23 min, respectively.

These observed results are related to the compositional, structural and electronic differences between the two materials. It is possible to notice that the higher proportion of the $Na_2Ti_3O_7$ phase in the structure favors the photocatalytic activity under visible irradiation. The difference in the photocatalytic performance of our experimental results using different irradiation light can be explained and supported by our theoretical simulations. As can be seen in the density of states in Fig. 9a, the band structure of $Na_2Ti_3O_7$ has an intragap in the conduction band, and is located near at 4.9 eV above the valence band maximum. Herewith, as the electron energy state is discrete and quantized, this region can be poorly occupied by photoexcited electrons due to its low density of states. Since the maximum intensity emission of the used ultraviolet lamp is in 254 nm (λ_{max}), its correspondent energy is 4.88 eV, which is close to the intragap region. Therefore, the $Na_2Ti_3O_7$ has a low photocatalytic activity under ultraviolet irradiation due to the low density of electrons that can be excited in its structure, decreasing the generation of electron-hole pairs. However, due to the lower energy of light emission of visible lamp compared to ultraviolet light, the electrons in the valence band maximum of $Na_2Ti_3O_7$ can be photoexcited and occupy the first band of its conduction band, which increases its photocatalytic activity under visible light irradiation. In contrast, the structure of the conduction band of the $H_2Ti_3O_7$ is composed of a high density of states, resulting in a *continuum* of energy states that can be easily occupied by photoexcited electron from its valence band maximum under ultraviolet irradiation. Since the energy of these photoexcited electrons is of approximately 4.9 eV, for the recombination of electron-hole pair, these electrons can transit between a high density of states in several pathways for the electron momentum relaxation before the recombination, which decreases the recombination rate and hence the photocatalytic activity. Under visible light irradiation, the photoexcited electrons can occupy a lower energy state in the conduction band, resulting in a lower density of states for the electronic transitions before the recombination of electron-hole pair, possible increasing its recombination rate.

One of the most useful approaches to evaluate electronic transitions in heterojunctions is the band alignment [85,86]. This method consists of analyzing the electronic behavior in the valence band maximum (VBM) and conduction band minimum (CBM) energies of the interface between the materials. In order to better investigate the photocatalytic mechanism occurring in the heterojunctions, theoretical and experimental energy band diagrams were performed. Fig. 11a illustrates an electronic model for the representation of predicted band gap alignment of the $H_2Ti_3O_7/Na_2Ti_3O_7$ system. From a theoretical point of view and based on band energy offsets of the models, the heterostructures showed to be a type-II structure. For instance, the $H_2Ti_3O_7/Na_2Ti_3O_7$ interface electronic structure has the electron and hole energies located at 1.01 eV and 1.08 eV, respectively. The CB and VB of the $H_2Ti_3O_7$ are below CB and VB of the $Na_2Ti_3O_7$, resulting in a staggered gap. The calculated effective bandgap is 2.16 eV, which was obtained by the difference between the CB of the $H_2Ti_3O_7$ and the VB of $Na_2Ti_3O_7$.

It is essential to highlight that the simulations were performed at 0 K, simulating perfect materials, without defects, and without boundary conditions. However, it is known that many factors can experimentally influence the interface between the two materials, such as grain orientation, crystal structure, structural defects, crystallinity and others [87,88]. For this reason, changing the parameter of the synthesis in the present study, the experimental band gap of the structures was changed and directly influenced the interface. According to the experimental and theoretical results, increasing the hydrogen concentration (more hydrogen energy levels can be added in the bandgap area) closes the effective band gap of the heterostructure, which can be experimentally observed in the band gap difference between NT-H2O and NT-HCl samples.

The results found in this study on the differences in photocatalytic efficiency of the NT-H_2O and NT-HCl samples on the different excitation energies used during photocatalysis can be unveiled by the PL analyses. According to the deconvolution results, the NT-H_2O sample presented a higher proportion of intermediate energy levels within the band gap. This favors the absorption of visible light due to the lower

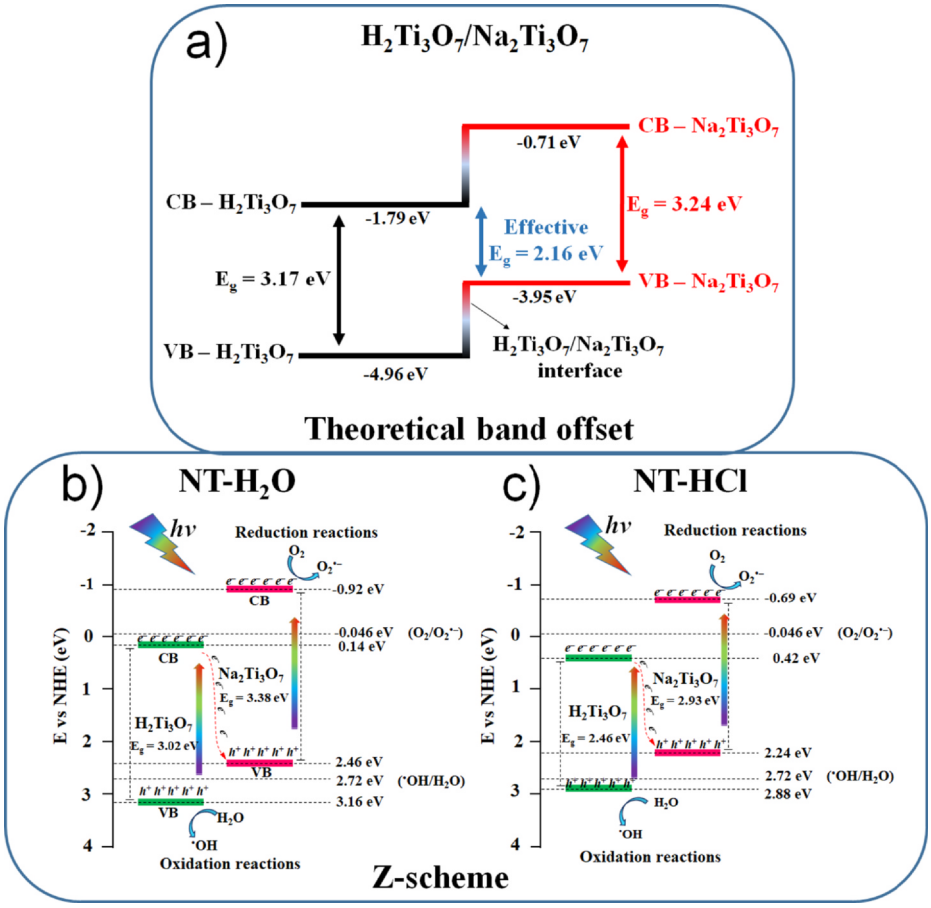

Fig. 11. a) Theoretical band offset and **b)** experimental Z-scheme mechanism for photocatalytic heterojunctions.

energy differences for electronic excitation than the band-band electronic transition. In contrast, the NT-HCl sample presented the majority of the band-band electronic transitions with lower proportion of intermediate energy states, hampering the visible light absorption and favoring the UV light absorption due to the direct band-band electronic transitions.

In order to investigate the charge carriers transfer mechanism in the heterojunctions for photocatalytic discoloration of Rh-B, experimental energy band diagrams for both samples were constructed according to the Mulliken electronegativity and the Equations (6) and (7) [89,90].

$$E_{VB} = \chi - E_e + 0.5E_g \quad (6)$$

$$E_{CB} = E_{VB} - E_g \quad (7)$$

In these equations, E_{VB} and E_{CB} are the energy of the valence band maximum and of the conduction band minimum, χ is the Mulliken electronegativity, *i.e.* the geometric mean of the electronegativity of the constituent atoms of the material, E_g is the experimental band gap energy and E_e is the energy of free electron in the hydrogen scale (4.5 eV). The calculated values of χ for $H_2Ti_3O_7$ and $Na_2Ti_3O_7$ are 6.15 eV and 5.27 eV, respectively. Considering the experimental band gap energies obtained by diffuse reflectance spectroscopy, the values of VB and CB for $H_2Ti_3O_7$ in the NT-H_2O sample are 3.16 eV and 0.14 eV, respectively, whereas the VB and CB values for $Na_2Ti_3O_7$ are 2.46 eV and −0.92 eV, respectively. In the NT-HCl sample, the calculated VB and CB values for $H_2Ti_3O_7$ are 2.89 eV and 0.42 eV, respectively, whereas the VB and CB values for $Na_2Ti_3O_7$ are 2.24 eV and −0.69 eV, respectively.

Fig. 11b and Fig. 11c show the energy band diagrams for the NT-H_2O and NT-HCl samples, respectively. As can be seen for both samples, the valence and conduction bands of $Na_2Ti_3O_7$ present lower potentials compared to the potentials of valence and conduction bands of $H_2Ti_3O_7$. For both samples, the band offset of the heterojunctions is a staggered gap, as predicted by theoretical simulations.

However, despite the conventional charge carrier transfer mechanism in the type II heterojunction that could occur in the interface, this type of charge carrier transfer is not the active mechanism for the photodiscoloration of the heterojunctions obtained. Regarding the reaction potentials [91,92] in photocatalytic process, a possible mechanism that explains the charge carrier transfer in $H_2Ti_3O_7/Na_2Ti_3O_7$ heterojunctions is the Z-scheme [93]. In this mechanism, electrons are photoexcited from VB to CB of $H_2Ti_3O_7$, and then migrate to the VB of $Na_2Ti_3O_7$ structure. Once these electrons are transferred to VB of $Na_2Ti_3O_7$, they are successively photoexcited to the CB of this structure. In this sense, the recombination rate in the $H_2Ti_3O_7$ structure is decreased, resulting in a hole-rich VB of $H_2Ti_3O_7$ and an electron-rich CB of $Na_2Ti_3O_7$.

Therefore, the water oxidation to form hydroxyl radicals as well as direct oxidation of Rh-B molecules occur at the VB of $H_2Ti_3O_7$ structure, whereas reduction of dissolved molecular oxygen to form superoxide radicals occurs at the CB of $Na_2Ti_3O_7$. The photocatalytic process occurring in the heterojunction samples are described in the Equations 8–16.

$$H_2Ti_3O_7 + h\nu \rightarrow H_2Ti_3O_{7(h\text{-VB})} + H_2Ti_3O_{7(e\text{-CB})} \quad (8)$$

$$Na_2Ti_3O_7 + h\nu \rightarrow Na_2Ti_3O_{7(h\text{-VB})} + Na_2Ti_3O_{7(e\text{-CB})} \quad (9)$$

$$H_2Ti_3O_{7(e\text{-CB})} + Na_2Ti_3O_{7(h\text{-VB})} \rightarrow H_2Ti_3O_7 + Na_2Ti_3O_7 \quad (10)$$

$$Na_2Ti_3O_{7(e\text{-CB})} + O_2 \rightarrow O_2^{\bullet-} + Na_2Ti_3O_7 \quad (11)$$

$$H_2Ti_3O_{7(h\text{-VB})} + H_2O \rightarrow H_2Ti_3O_7 + HO^{\bullet} + H^+ \quad (12)$$

$$O_2^{\bullet-} + H^+ \rightarrow HO_2^{\bullet} \quad (13)$$

$$HO^{\bullet} + \text{Rh-B} \rightarrow \text{COC} + CO_2 + H_2O \quad (14)$$

$$HO_2^{\bullet} + \text{Rh-B} \rightarrow \text{COC} + CO_2 + H_2O \quad (15)$$

$$H_2Ti_3O_{7(h\text{-VB})} + \text{Rh-B} \rightarrow \text{COC} + CO_2 + H_2O \quad (16)$$

As stated in Equations (10) and (11), the $H_2Ti_3O_7$ and $Na_2Ti_3O_7$ phases are excited by incident photons ($h\nu$), generating the photoexcited electrons and holes in the conduction and valence bands, respectively, in each phase. The photoexcited electron in the conduction band of $H_2Ti_3O_7$ migrates to the valence band of $Na_2Ti_3O_7$ (Equation (10)). The photoexcited electron in the CB of $Na_2Ti_3O_3$ reduces O_2 to form $O_2^{\bullet-}$ (Equation (11)) and a photogenerated hole in the VB of $H_2T_3O_7$ oxidizes H_2O to form $HO^{\bullet}$ and H^+ (Equation (12)). The reaction between $O_2^{\bullet-}$ and H^+ generates a reactive species able to oxidize organic compounds, the hydroperoxyl radical ($HO_2^{\bullet}$) (Equation (13)). Herein, the generated reactive oxygen species, $HO^{\bullet}$ and $HO_2^{\bullet}$, along with the holes in the VB of $H_2Ti_3O_7$ can oxidize the Rh-B molecules to form colorless organic compounds (COC), CO_2 and H_2O. Therefore, the formation of the heterojunction between $H_2Ti_3O_7$ and $Na_2Ti_3O_7$ phases in the same nanotube results in a Z-scheme mechanism for photodiscoloration of the Rh-B solution.

4. Conclusions

The washing process of titanate nanotubes with water and HCl obtained by the microwave-assisted hydrothermal method proved to be an important synthesis parameter to control the phase content and heterojunction structure, as it favored the cation exchange reaction in the nanotubes. Both samples presented nanotube morphology, differing only in wall thickness and the inner diameter of the tube. The nanotubes obtained are composed of $H_2Ti_3O_7$ and $Na_2Ti_3O_7$ phases in the same particle due to the cation exchange reaction, as observed by TEM analyses. Both crystalline phases showed varying content in each sample, being that the sample washed with HCl showed a higher proportion of the $H_2Ti_3O_7$ phase compared to the sample washed with water. The PL spectra analyses indicated that the sample washed with water presented a higher proportion of defects states than the sample washed with HCl, corroborating the theoretical calculations of surface termination, in which the (1–11) surface of $Na_2Ti_3O_3$ has a higher content of oxygen vacancies than (1–10) surface of $H_2Ti_3O_7$. This higher proportion of defects indicates that a higher efficiency was induced in the sample washed with water under visible light irradiation compared to the sample washed with HCl, which had a higher efficiency in UV light due to the majority of the band-band electronic transitions, favoring the UV light absorption. Theoretical and experimental calculations indicated a staggered gap between the heterojunction of both phases, in which the heterojunction formed presented a photocatalytic mechanism governed by the Z-scheme model for charge carrier transfer. In this sense, this work demonstrated the importance of the washing process to favor the cation exchange reaction for the formation of heterojunction material in the same particle. It also allowed investigation of the photocatalytic mechanism involved between both phases for degradation of organic compounds. Herewith, it is demonstrated that the washing process is an important parameter to modulate the phase content and hence the properties of heterojunction materials for the development of devices with desirable properties.

CRediT authorship contribution statement

Isabela M. Iani: Methodology, Investigation, Writing - original draft. **Vinícius Teodoro:** Data curation, Writing - review & editing. **Naiara L. Marana:** Software, Writing - review & editing. **Ubirajara Coleto:** Writing - original draft. **Julio R. Sambrano:** Visualization, Writing - review & editing. **Alexandre Z. Simões:** Visualization, Writing - review & editing. **Marcio D. Teodoro:** Visualization, Writing - review & editing. **Elson Longo:** Resources, Visualization. **Leinig A. Perazolli:** Resources, Writing - review & editing. **Rafael A. C. Amoresi:** Investigation, Supervision, Writing - review & editing. **Maria Aparecida Zaghete:** Resources, Conceptualization, Methodology, Supervision.

Declaration of Competing Interest

The authors declare that they have no known competing financial interests or personal relationships that could have appeared to influence the work reported in this paper.

Acknowledgments

The authors acknowledge the CEPID/CDMF and the São Paulo Research Foundation (FAPESP) (Prof. Nos. 2013/07296-2, 2018/01914-0, 2017/19143-7, 2019/08928-9, 2016/25500-4, 2019/12430-6, 2017/24405-0 and 2019/12114-7), National Council for Scientific and Technological Development (CNPq) (No 142035/2017-3), and the Coordenação de Aperfeiçoamento de Pessoal de Nível Superior (CAPES) for the financial support granted in the course of this research. We are also grateful to the LMA-IQ for providing the FEG-FIB-SEM facilities. To Emily Mary Grandoli, native English speaker, for reviewing the translation of this text.

Appendix A. Supplementary data

Supplementary data to this article can be found online at https://doi.org/10.1016/j.apsusc.2020.148137.

References

[1] A. Koltsakidou, Z. Terzopoulou, G.Z. Kyzas, D.N. Bikiaris, D.A. Lambropoulou, Biobased Poly(ethylene furanoate) polyester/TiO_2 supported nanocomposites as effective photocatalysts for anti-inflammatory/analgesic drugs, Molecules 24 (3) (2019) 564, https://doi.org/10.3390/molecules24030564.
[2] Y. Ye, H. Bruning, X. Li, D. Yntema, H.H. Rijnaarts, Significant enhancement of micropollutant photocatalytic degradation using a TiO_2 nanotube array photoanode based photocatalytic fuel cell, Chem. Eng. J. 354 (2018) 553–562, https://doi.org/10.1016/j.cej.2018.08.064.
[3] A.A. Isari, A. Payan, M. Fattahi, S. Jorfi, B. Kakavandi, Photocatalytic degradation of rhodamine B and real textile wastewater using Fe-doped TiO_2 anchored on reduced graphene oxide (Fe-TiO_2/rGO): Characterization and feasibility, mechanism and pathway studies, Appl. Surf. Sci. 462 (2018) 549–564, https://doi.org/10.1016/j.apsusc.2018.08.133.
[4] A. Sandoval, C. Hernández-Ventura, T.E. Klimova, Titanate nanotubes for removal of methylene blue dye by combined adsorption and photocatalysis, Fuel 198 (2017) 22–30, https://doi.org/10.1016/j.fuel.2016.11.007.
[5] J.E. Yoo, A.A. Alshehri, S. Qin, S.M. Bawaked, M.M.M. Mostafa, N. Katabathini, D. Fehn, J. Schmidt, A. Mazare, A. Denisov, G. Cha, K. Meyerm, P. Schmuki, Establishing high photocatalytic H_2 evolution from multiwalled titanate nanotubes, Chem. Cat. Chem. 12 (2020) 1–7, https://doi.org/10.1002/cctc.202000281.
[6] R. Li, X. Li, C. Liu, M. Ye, Q. Yang, Z. Liu, L. Xie, G. Yang, Enhanced electron transport through a nanoforest-like structure of CoNi nanoalloy@nitrogen-doped carbon nanotubes for highly efficient catalysis of overall water splitting, Appl. Surf. Sci.. 517 (2020) 145841, https://doi.org/10.1016/j.apsusc.2020.145841.
[7] T.G. Kim, E. Samuel, C.W. Park, B. Joshi, M.W. Kim, M.T. Swihart, S.S. Yoon, Supersonically sprayed Zn_2SnO_4/SnO_2/carbon nanotube films for high-efficiency water splitting photoanodes, J. Alloy. Compd. 828 (2020) 154374, https://doi.org/10.1016/j.jallcom.2020.154374.
[8] J. Kang, Y. Jung, Free-standing sulfur-carbon nanotube electrode with a deposited sulfur layer for high-energy lithium-sulfur batteries, J. Nanosci. Nanotechnol. 20 (8) (2020) 5019–5023, https://doi.org/10.1166/jnn.2020.17847.
[9] J.W. Park, H. Park, J. Kang, S. Kim, Y. Jung, Carbon nanotube-based sulfur cathode with a mesoporous carbon-silica composite for long cycle life Li-S batteries, J. Nanosci. Nanotechnol. 20 (8) (2020) 4949–4954, https://doi.org/10.1166/jnn.2020.17851.
[10] P. Weichi, L. Haiyang, Z. Xuenjing, Z. Wenming, S. Ebrahimi, AlN nanotubes and nanosheets as anode material for K-ion batteries: DFT studies, Pyhs. Lett. A. 384 (18) (2020) 126396, https://doi.org/10.1016/j.physleta.2020.126396.
[11] J. Bai, Y.L. Luo, B. An, Q. Wang, X. Cheng, J. Li, X. Pan, J. Zhou, Y. Wang, E. Xie, Ni/Au bimetal decorated In_2O_3 nanotubes for ultra-sensitive ethanol detection, Sensor Actuat. B-Chem. 311 (2020) 127938, https://doi.org/10.1016/j.snb.2020.127938.

[12] S. Rezaie, Z.G. Bafghi, N. Manavizadeh, Carbon-doped ZnO nanotube-based highly effective hydrogen gas sensor: a first-principles study, Int. J. Hydrogen Energ. 45 (27) (2020) 14174–14782, https://doi.org/10.1016/j.ijhydene.2020.03.050.

[13] X. Zeng, L. Liu, Y. Lv, B. Zhao, X. Ju, S. Xu, J. Zhang, C. Tian, D. Sun, X. Tang, Ultrasensitive and fast response formaldehyde sensor based on La_2O_3-In_2O_3 beaded nanotubes at low temperature, Chem. Phys. Lett. 746 (2020) 137289, https://doi.org/10.1016/j.cplett.2020.137289.

[14] S. Chen, L. Zhao, W. Wei, Y. Li, L. Mi, A novel strategy to synthesize NiCo layered double hydroxide nanotube from metal organic framework composite for high-performance supercapacitor, J. Alloy. Compd. 831 (2020) 154794, https://doi.org/10.1016/j.jallcom.2020.154794.

[15] Y. Li, C. Song, J. Chen, X. Shang, J. Chen, Y. Li, M. Huang, F. Meng, Sulfur and nitrogen Co-doped activated $CoFe_2O_4$@C nanotubes as an efficient material for supercapacitor applications, Carbon 162 (2020) 124–135, https://doi.org/10.1016/j.carbon.2020.02.050.

[16] A. Liu, J. Tang, Construction of polypyrrole-wrapped hierarchical $CoMoO_4$ nanotubes as a high-performance electrode for supercapacitors, Ceram. Inter. 16 (8) (2020) 10893–11080, https://doi.org/10.1016/j.ceramint.2020.01.103.

[17] M.M. Ovhal, N. Kumar, S. Hong, H. Lee, J. Kang, Asymmetric supercapacitor featuring carbon nanotubes and nickel hydroxide grown on carbon fabric: A study of self-discharging characteristics, J. Alloy. Compd. 828 (2020) 154447, https://doi.org/10.1016/j.jallcom.2020.154447.

[18] Y. Diao, M. Yan, X. Li, C. Zhou, B. Peng, H. Chen, H. Zhang, In-situ grown of g-C_3N_4/Ti_3C_2/TiO_2 nanotube arrays on Ti meshes for efficient degradation of organic pollutants under visible light irradiation, Colloid. Surface. A 594 (2020) 124511, https://doi.org/10.1016/j.colsurfa.2020.124511.

[19] P. Gao, Z. Yin, Y. Liu, Z. Du, Z. Duan, L. Zhang, Solvothermal synthesis of multiwall carbon nanotubes/BiOI photocatalysts for the efficient degradation of antipyrine under visible light, Environ. Res. 185 (2020) 109468, https://doi.org/10.1016/j.envres.2020.109468.

[20] M. Ji, J. Di, Y. Liu, R. Chen, K. Li, Z. Chen, J. Xia, H. Li, Confined active species and effective charge separation in $Bi_4O_5I_2$ ultrathin hollow nanotube with increased photocatalytic activity, Appl. Catal. B-Environ. 268 (2020) 118403, https://doi.org/10.1016/j.apcatb.2019.118403.

[21] M. Hinojosa-Reyes, R. Camposeco-Solis, F. Ruiz, $H_2Ti_3O_7$ titanate nanotubes for highly effective adsorption of basic fuchsin dye for water purification, Micropor. Mesopor. Mat. 276 (2019) 183–191, https://doi.org/10.1016/j.micromeso.2018.09.035.

[22] A.H. Zaki, M. Lee, Effects of K^+, Mg^{2+}, Ca^{2+}, Zn^{2+}, La^{3+}, Cr^{3+}, Ce^{3+}, Ce^{4+}, and Mo^{5+} doping on the adsorption performance and optical properties of sodium titanate nanotubes, ACS Omega 4 (2019) 19623–19634, https://doi.org/10.1021/acsomega.9b02229.

[23] S. Shen, C. Wang, M. Sun, M. Jia, Z. Tang, J. Yang, Free-standing sodium titanate ultralong nanotube membrane with oil-water separation, self-cleaning, and photocatalysis properties, Nanoscale Res. Lett. 15 (2020) 22, https://doi.org/10.1186/s11671-020-3255-9.

[24] J.S. Souza, W.A. Alvez, Influence of preparation methodology on the photocatalytic activity of nitrogen doped titanate and TiO_2 nanotubes, J. Nanosci. Nanotechnol. 20 (9) (2020) 5390–5401, https://doi.org/10.1166/jnn.2020.17304.

[25] L.F. Garay-Rodrigues, S.M. López, T. Andreu, E. Moctezuma, Photocatalytic hydrogen evolution using bi-metallic (Ni/Pt) $Na_2Ti_3O_7$ whiskers: effect of the deposition order, Catalysts. 9 (3) (2019) 285, https://doi.org/10.3390/catal9030285.

[26] S. Preda, C. Anastasescu, I. Balint, P. Umek, M. Sluban, C.C. Negrila, D.G. Angelescu, V. Bratan, A. Rusu, M. Zaharescu, Charge separation and ROS generation on tubular sodium titanates exposed to simulated solar light, Appl. Surf. Sci.. 470 (2019) 1053–1063, https://doi.org/10.1016/j.apsusc.2018.11.194.

[27] X. Zhu, A. Anzai, A. Yamamoto, H. Yoshida, Silver-loaded sodium titanate photocatalysts for selective reduction of carbon dioxide to carbon monoxide with water, Appl. Catal. B-Environ. 243 (2019) 47–56, https://doi.org/10.1016/j.apcatb.2018.10.021.

[28] T. Kasuga, M. Hiramatsu, A. Hoson, T. Sekino, K. Niihara, Formation of titanium oxide nanotube, Langmuir 14 (1998) 3160–3163, https://doi.org/10.1021/la9713816.

[29] T. Kasuga, M. Hiramatsu, A. Hoson, T. Sekino, K. Niihara, Titania nanotubes prepared by chemical processing, Adv. Mater. 11 (15) (1999) 1307–1311, https://doi.org/10.1002/(SICI)1521-4095(199910)11:15<1307::AID-ADMA1307>3.0.CO;2-H.

[30] D.V. Bavykin, J.M. Friederich, F.C. Walsh, Protonated titanates and TiO_2 nanostructured materials: synthesis, properties, and applications, Avd. Mater. 18 (2006) 2807–2824, https://doi.org/10.1002/adma.200502696.

[31] C.-C. Chung, T.-W. Chung, T.-C.-K. Yang, Rapid synthesis of titania nanowires by microwave-assitsed hydrothermal, Ind. Eng. Chem. 47 (2008) 2301–2307, https://doi.org/10.1021/ie0713644.

[32] S.B.S. Gusmão, A. Ghosh, T.M.F. Marques, O.P. Ferreira, A.O. Lobo, J.A.O. Osajima, C. Luz-Lima, R.R.M. Souza, J.M.E. Matos, B.C. Viana, One-pot synthesis of titanate nanotubes decorated with anatase nanoparticles using a microwave-assisted hydrothermal reaction, J. Nanomater. 1 (2019) 1–10, https://doi.org/10.1155/2019/4825432.

[33] S. Parida, S.K. Rout, L.S. Cavalcante, A.Z. Simões, P.K. Barhai, N.C. Batista, E. Longo, M. Siu Li, S.K. Sharma, Structural investigation and improvement of photoluminescence properties in $Ba(Zr_xTi_{1-x})O_3$ powders synthesized by the solid state reaction method, Mater. Chem. Phys. 142 (2013) 70–76, https://doi.org/10.1016/j.matchemphys.2013.06.041.

[34] U. Coleto, R.A.C. Amoresi, V. Teodoro, I.M. Iani, E. Longo, M.A. Zaghete, L.A. Perazolli, An approach for photodegradation mechanism at TiO_2/$SrTiO_3$ interface, J. Mater. Sci.: Mater. Elétron. 29 (2019) 20329–20338, https://doi.org/10.1007/s10854-018-0167-x.

[35] W. Zhao, Y. Feng, H. Huang, P. Zhou, J. Li, L. Zhang, B. Dai, J. Xu, F. Zhu, N. Sheng, D.Y.C. Leung, A novel Z-scheme Ag_3VO_4/$BiVO_4$ heterojunction photocatalyst: study on the excellent photocatalytic performance and photocatalytic mechanism, Appl. Catal. B-Environ. 245 (2019) 448–458, https://doi.org/10.1016/j.apcatb.2019.01.001.

[36] C. Zhao, L. Tian, Z. Zou, Z. Chen, H. Tang, Q. Liu, Z. Lin, X. Yang, Revealing and accelerating interfacial charge carrier dynamics in Z-scheme heterojunctions for highly efficient photocatalytic oxygen evolution, Appl. Catal. B-Environ. 268 (2020) 118445, https://doi.org/10.1016/j.apcatb.2019.118445.

[37] W. Liu, J. Shen, X. Yang, Q. Liu, H. Tang, Dual Z-scheme g-C_3N_4/Ag_3PO_4/Ag_2MoO_4 ternary composite photocatalyst for solar oxygen evolution from water splitting, Appl. Surf. Sci. 456 (2018) 369–378, https://doi.org/10.1016/j.apsusc.2018.06.156.

[38] X. Yang, L. Tian, X. Zhao, H. Tang, Q. Liu, G. Li, Interfacial optimization of g-C_3N_4-based Z-scheme heterojunction toward synergistic enhancement of solar-driven photocatalytic oxygen evolution, Appl. Catal. B-Environ. 244 (2019) 240–249, https://doi.org/10.1016/j.apcatb.2018.11.056.

[39] L. Tian, X. Yang, X. Cui, Q. Liu, H. Tang, Fabrication of dual direct Z-scheme g-C_3N_4/MoS_2/Ag_3PO_4 photocatalyst and its oxygen evolution performance, Appl. Surf. Sci. 463 (2019) 9–17, https://doi.org/10.1016/j.apsusc.2018.08.209.

[40] H.T.S. Souza, S.A.A. Oliveira, J.S. Souza, Modulating the photocatalytic activity of Ag nanoparticles-titanate nanotubes heterojunctions through control of microwave-assisted synthesis conditions, J. Photoch. Photobio. A. 390 (2020) 112264, https://doi.org/10.1016/j.jphotochem.2019.112264.

[41] S. Muniyappan, T. Solaiyammal, K. Sudhakar, A. Karthigeyan, P. Murugakoothan, Conventional hydrothermal synthesis of titanate nanotubes: systmatic discussions on structural, optical, thermal and morphological properties, Mod. Eletron. Mater. 3 (2017) 174–178, https://doi.org/10.1016/j.moem.2017.10.002.

[42] D.C. Manfroi, A. Dos Anjos, A.A. Cavalheiro, L.A. Perazolli, J.A. Varela, M.A. Zaghete, Titanate nanotubes produced from microwave-assisted hydrothermal synthesis: photocatalytic and structural properties, Ceram. 40 (9) (2014) 14483–14491, https://doi.org/10.1016/j.ceramint.2014.07.007.

[43] J. Andrés, L. Gracia, A.F. Gouveia, M.M. Ferrer, E. Longo, Effects of surface stability on the morphological transformation of metals and metal oxides as investigated by first principles calculations, Nanotechnology. 26 (40) (2015) 405703, https://doi.org/10.1088/0957-4484/26/40/405703.

[44] J. Suetake, A.Y. Nosaka, K. Hodouchi, H. Matsubara, Y. Nosaka, Characteristics of titanate nanotube and the states of the confined sodium ions, J. Phys. Chem. C 112 (2008) 18474–18482, https://doi.org/10.1021/jp8069223.

[45] W. Hu, L. Li, G. Li, J. Meng, W. Tong, Synthesis of titanate-based nanotubes for one-dimensionally confined electrical properties, Phys. Chem. C. 113 (2009) 16996–17001, https://doi.org/10.1021/jp907001n.

[46] N.H. Nguyen, H. Bai, Effect of washing pH on the properties of titanate nanotubes and itsactivity for photocatalytic oxidation of NO and NO_2, Appl. Surf. Sci. 355 (2015) 672–680, https://doi.org/10.1016/j.apsusc.2015.07.118.

[47] C. Zhou, C. Lai, C. Zhang, G. Zeng, D. Huang, M. Cheng, L. Hu, W. Xiong, M. Chen, J. Wang, Y. Yang, L. Jiang, Semiconductor/boron nitride composites: synthesis, properties, and photocatalysis applications, Appl. Catal. B-Environ. 238 (2018) 6–18, https://doi.org/10.1016/j.apcatb.2018.07.011.

[48] X. Yu, T.J. Marks, A. Facchetti, Metal oxides for optoelectronic applications, Nat. Mater. 15 (2016) 383–396, https://doi.org/10.1038/nmat4599.

[49] Y. Lv, S. Duan, R. Wang, Structure design, controllable synthesis, and application of metal-semiconductor heterostructure nanoparticles, Prog. Nat. Sci-Mater. 30 (2020) 1–12, https://doi.org/10.1016/j.pnsc.2019.12.005.

[50] K. Anand, J. Kaur, R.C. Singh, R. Thangaraj, Preparation and characterization of Ag-doped In_2O_3 nanoparticles gas sensor, Chem. Phys. Lett. 682 (2017) 140–146, https://doi.org/10.1016/j.cplett.2017.06.008.

[51] T. Kasuga, Formation of titanium oxide nanotubes using chemical treatments using chemical treatments and their characteristic properties, Thin Solid Films 496 (2016) 141–145, https://doi.org/10.1016/j.tsf.2005.08.341.

[52] R. Demichelis, B. Civalleri, M. Ferrabone, R. Dovesi, On the performance of eleven DFT functionals in the description of the vibrational properties of aluminosilicates, Inter. J. Quuantum Chem. 110 (2) (2010) 406–415, https://doi.org/10.1002/qua.22301.

[53] A. Erba, J. Baima, I. Bush, R. Orlando, R. Dovesi, Large-scale condensed matter DFT simulations: performance and capabilities of the CRYSTAL code, J. Chem. Theory Comput. 13 (2017) 5019–5027, https://doi.org/10.1021/acs.jctc.7b00687.

[54] R. Dovesi, C. Roetti, C.F. Fava, M. Prencipe, V.R. Saunders, On the elastic properties of lithium, sodium an potassium oxide. An ab initio study, Chem. Phys. 156 (1991) 11–19, https://doi.org/10.1016/0301-0104(91)87032-Q.

[55] T. Bredow, P. Heitjans, M. Wilkening, Electric field gradient calculations for Li_xTiS_2 and comparison with Li-7 NMR results, Phys. Rev. B. 70 (2004) 115111, https://doi.org/10.1103/PhysRevB.70.115111.

[56] T. Bredow, K. Jug, R.A. Evarestov, Electronic and magnetic structure of $ScMnO_3$, Phys. Status Solidi B 243 (2016) R10–R12, https://doi.org/10.1002/pssb.200541403.

[57] R. Dovesi, E. Ermondi, E. Ferrero, C. Pisani, C. Roetti, Hartree-Fock study of lithium hydride with the use of a polarizable basis set, Phys. Rev. B. 29 (1983) 3591–3600, https://doi.org/10.1103/PhysRevB.29.3591.

[58] S. Andersson, A.D. Wadsley, The crystal structure of $Na_2Ti_3O_7$, Acta Crystallogr. 14 (1961) 1245–1249, https://doi.org/10.1107/S0365110X61003636.

[59] O.V. Yakubovich, V.V. Kireev, Refinement of the crystal structure of $Na_2Ti_3O_7$, Cryst. Rep. 48 (2003) 24–28, https://doi.org/10.1134/1.1541737.

[60] S. Zhang, Q. Chen, L.-M. Peng, Structure and formation of $H_2Ti_3O_7$ nanotubes in an alkali environment, Phys. Rev. B: Condens. Matter 71 (1) (2005) 014104, https://

doi.org/10.1103/PhysRevB.71.014104.
[61] X.G. Xu, X. Ding, Q. Chen, L.-M. Peng, Electronic, optical, and magnetic properties of Fe-intercalated $H_2Ti_3O_7$ nanotubes: First-principles calculations and experiments, Phys. Rev. B. 73 (16) (2006), https://doi.org/10.1103/PhysRevB.73.165403.
[62] A.A. Araújo-Filho, F.L.R. Silva, A. Righi, M.B. da Silva, B.P. Silva, E.W.S. Caetano, V.N. Freire, Structural, electronic and optical properties of monoclinic $Na_2Ti_3O_7$ from density functional theory calculations: A comparison with XRD and optical absorption measurements, J. Solid State Chem. 250 (2017) 68–74, https://doi.org/10.1016/j.jssc.2017.03.017.
[63] J.B. Rivest, P.K. Jain, Cation exchange on the nanoscale: an emerging technique for new material synthesis, device fabrication, and chemical sensing, Chem. Soc. Rev. 42 (2013) 89–96, https://doi.org/10.1039/c2cs35241a.
[64] J.B. Rivest, S.L. Swisher, L.-K. Fong, H. Zheng, A.P. Alivisatos, Assembled monolayer nanorod heterojunctions, ACS Nano 5 (2005) 3811–3816, https://doi.org/10.1021/nn2001454.
[65] W. Borchardt-Ott, Crystallography: An Introduction, third ed., Edimburgo: Springer, Altenberge, 2011. https://doi.org/10.1007/978-3-642-16452-1.
[66] P.E. Rubavathi, L. Venkidu, M.V.G. Babu, R.V. Raman, B. Bagyalakshmi, S.M.A. Kader, K. Baskar, M. Muneeswaran, N.V. Giridharan, B. Sundarakannan, Structure, morphology and magnetodielectric investigations of $BaTi_{1-x}Fe_xO_{3-\delta}$ ceramics, J. Mater. Sci.: Mater. Electron. 30 (2019) 5706–5717, https://doi.org/10.1007/s10854-019-00864-6.
[67] W. Elsayed, S. Abdalla, N. Seriani, Quasiparticle and optical properties of hydrogen titanate and its defective systems: an investigation by density functional theory with hubbard correction, many-body perturbation theory, and bethe-salpeter equation, Physica Status Solidi (b) 257 (3) (2019) 1900054, https://doi.org/10.1002/pssb.201900054.
[68] A.S. Malik, T. Liu, M. Dupuis, R. Li, C. Li, Water oxidation on TiO_2: a comparative DFT study of $1e^-$, $2e^-$, and $4e^-$ processes on rutile anatase, and brookite, J. Phys. Chemistry C 124 (2020) 8094–8100, https://doi.org/10.1021/acs.jpcc.9b11450.
[69] W.T. Wallace, B.K. Min, D.W. Goodman, The stabilization of supported gold clusters by surface defects, J. Mol. Catal. A: Chem. 228 (2005) 3–10, https://doi.org/10.1016/j.molcata.2004.09.085.
[70] H.M. Kim, F. Miyaji, T. Kokubo, Effect of heat treatment on apatite-forming ability of Ti metal induced by alkali treatment, J. Mater. Sci. – Mater. Med. 8 (1997) 341–347, https://doi.org/10.1023/A:1018524731409.
[71] D.V. Bavykin, J.M. Friedrich, A.A. Lapkin, F.C. Walsh, Stability of aqueous suspensios of titanate nanotubes, Chem. Mater. 18 (2006) 1124–1129, https://doi.org/10.1021/cm0521875.
[72] L. Qian, Z. Du, S. Yang, S. Jin, Raman study of titania nanotube by soft chemical process, J. Mol. Struct. 749 (2005) 103–107, https://doi.org/10.1016/j.molstruc.2005.04.002.
[73] B.C. Viana, O.P. Ferreira, A.G. Souza Filho, A.A. Hidalgo, J. Mendes Filho, O.L. Alves, Alkali metal intercalated titanate nanotubes: A vibrational spectroscopy study, Vib. Spectrosc. 55 (2011) 183–187, https://doi.org/10.1016/j.vibspec.2010.11.007.
[74] P.H. Hipólito, N.J. Flores, E.M. Klimova, A.G. Cortés, X. Bokhimi, L.E. Alarcón, T.E. Klimova, Novel heterogeneous basic catalysts of biodiesel production: sodium titanate nanotubes doped with potassium, Catal. Today 250 (2015) 187–196, https://doi.org/10.1016/j.cattod.2014.03.025.
[75] S. Mozia, E. Borowiak-Palén, J. Przepiórski, B. Grzmil, T. Tsumura, M. Toyoda, J. Grzechulska-Damszel, A.W. Morawski, Physico-chemical properties and possible photocatalytic applications of titanate nanotubes synthesized via hydrothermal method, J. Phys. Chem. Solids 71 (3) (2010) 263, https://doi.org/10.1016/j.jpcs.2009.12.074.
[76] B.J. Wood, R.G.J. Strens, Diffuse reflectance spectra and optical properties of some sulphides and related minerals, Miner. Mag. 43 (1979) 509–518, https://doi.org/10.1180/minmag.1979.043.328.11.
[77] A. Sarkar, K. Karkamar, A.K. Singh, K. Mandal, G.G. Khan, Surface functionalized $H_2Ti_3O_7$ nanowires to engineer visible-light photoswitching, electrochemical water splitting, and photocatalysis, Pyhs. Chem. Chem. Phys. 18 (2016) 26900–26912, https://doi.org/10.1039/C6CP05154E.
[78] M.H. Razali, M.N.A. Fauzi, A.R. Mohamed, S. Sreekantan, Physical properties study of TiO_2 nanoparticle synthesis via hydrothermal method using TiO_2 microparticles as percursor, Adv. Mater. Res. 772 (2013) 365–370, https://doi.org/10.4028/www.scientific.net/AMR.772.365.
[79] R.A.C. Amoresi, V. Teodoro, G.F. Teixeira, M.S. Li, A.Z. Simões, L.A. Perazolli, E. Longo, M.A. Zaghete, Electrosteric colloidal stabilization for obtaining $SrTiO_3$/TiO_2 heterojunction: Microstructural evolution in the interface and photonics properties, J. Eur. Ceram. Soc. 38 (2018) 1621–1631, https://doi.org/10.1016/j.jeurceramsoc.2017.10.056.
[80] Y. Matsumoto, U. Unal, Y. Kimura, S. Ohashi, K. Izawa, Synthesis and photoluminescent properties of titanate layered oxides intercalated with lanthanide cations by electrostatic self-assembly methods, J. Phys. Chem. B 109 (2005) 12748–12754, https://doi.org/10.1021/jp8038048.
[81] U. Coleto Jr., R.A.C. Amoresi, C.A.M. Pereira, A.Z. Simões, M.A. Zaghete, E.S. Monteiro Filho, E. Longo, L.A. Perazolli, Influence of defects on photoluminescent and photocatalytic behavior of CaO/$SrTiO_3$ heterojunctions, Ceram. Int. 45 (2019) 15244–15251, https://doi.org/10.1016/j.ceramint.2019.05.013.
[82] V.M. Longo, A.T. Figueiredo, S. Lázaro, M.F. Gurgel, M.G.S. Costa, C.O. Paiva-Santos, J.A. Varela, E. Longo, V.R. Mastelaro, F.S. Vicente, A.C. Hernandes, R.W.A. Franco, Structural conditions that leads to photoluminescence emission in $SrTiO_3$: An experimental and theoretical approach, J. Appl. Phys. 104 (2008) 023515, https://doi.org/10.1063/1.2956741.
[83] P. Atkins, J. Paula, Físico-química, eighth ed., Rio de Janeiro, LTC, 2, 223-225, 2008.
[84] B. Liu, X. Zhao, C. Terashima, A. Fujishima, K. Nakata, Thermodynamic and kinetic analysis of heterogeneous photocatalysis for semiconductor systems, Phys. Chem. Chem. Phys. 16 (2014) 8751–8760, https://doi.org/10.1039/c3cp55317e.
[85] N.L. Marana, F.A. La Porta, E. Longo, J.R. Sambrano, Theoretical study on band alignment mechanism for the ZnO@ZnS interface of core-shell structures, Curr. Phys. Chem. 5 (4) (2016) 327, https://doi.org/10.2174/1877946805041603081709 20.
[86] D. Zhang, S. Dong, Challenges in band alignment between semiconducting materials: a case of rutile and anatase TiO_2, Prog. Nat. Sci-Mater. 29 (3) (2019) 277–284, https://doi.org/10.1016/j.pnsc.2019.03.012.
[87] G. Di Liberto, S. Tosoni, G. Pacchioni, Theoretical treatment of semiconductor heterojunctions for photocatalysis: the WO_3/$BiVO_4$ interface, J. Phys.: Condens. Matter 31 (434001) (2019), https://doi.org/10.1088/1361-648X/ab2fa4.
[88] P.-C. Chen, M. Liu, J.S. Du, B. Meckes, S. Wang, H. Lin, V.P. Dravid, C. Wolverton, C.A. Mirkin, Interface and heterostructure design in polyelemental nanoparticles, Science 363 (6430) (2019) 959–964, https://doi.org/10.1126/science.aav4302.
[89] I. Shahid, S. Ahmad, N. Shehzad, S. Yao, C.V. Nguyen, L. Zhang, Z. Zhou, Electronic and photocatalytic performance of boron phosphide-blue phosphorene vdW heterostructures, Appl. Surf. Sci. 523 (2020) 146483, https://doi.org/10.1016/j.apsusc.2020.146483.
[90] M. Lu, Q. Li, C. Zhang, X. Fan, L. Li, Y. Dong, G. Chen, H. Shi, Remarkable photocatalytic activity enhancement of CO_2 conversion over 2D/2D g-C_3N_4/$BiVO_4$ Z-scheme heterojunction promoted by efficient interfacial charge transfer, Carbon 160 (2020) 342–352, https://doi.org/10.1016/j.carbon.2020.01.038.
[91] G. Li, K.H. Wong, X. Zhang, C. Hu, R.C. Chan, P.K. Wong, Degradation of Acid Orange 7 using magnetic AgBr under visible light: the roles of oxidizing species, Chemosphere 79 (9) (2009) 1185–1191, https://doi.org/10.1016/j.chemosphere.2009.06.027.
[92] B. Wang, P. Zhang, J. Xia, S. Dai, H. Li, Ionic liquid-induced strategy for porous perovskite-like $PbBiO_2Br$ photocatalysts with enhanced photocatalytic activity and mechanism insight, Appl. Catal. B-Enviromen. 206 (2017) 127–135, https://doi.org/10.1016/j.apcatb.2016.12.049.
[93] Q. Xu, L. Zhang, J. Yu, S. Wageh, A.A. Al-Ghamdi, M. Jaroniec, Direct Z-scheme photocatalysts: Principles, synthesis, and applications, Mater. Today 21 (10) (2018) 1042–4063, https://doi.org/10.1016/j.mattod.2018.04.008.